micromachines

MDPI

Ariticle

A New Grinding Force Model for Micro Grinding RB-SiC Ceramics with Grinding Wheel Topography as an Input

Zhipeng Li[1,2], Feihu Zhang[1]*, Xichun Luo[2]*, XiaoGuang Guo[3], Yukui Cai[2], Wenlong Chang[2] and Jining Sun[4]

1 School of Mechatronics Engineering, Harbin Institute of Technology, Harbin, China; 13B908073@hit.edu.cn (Z.L.); zhangfh@hit.edu.cn (F.Z.)

2 Centre for Precision Manufacturing, DMEM, University of Strathclyde, Glasgow, UK; xichun.luo@strath.ac.uk (X.L.); yukui.cai@strath.ac.uk (Y.C.); wenlong.chang@strath.ac.uk (W.C.);

3 Key Laboratory for Precision and Non-Traditional Machining Technology, Dalian University of Technology, Dalian, China; guoxg@dlut.edu.cn (X.G.)

4 School of Engineering and Physical Science, Heriot Wat University, Edinburgh, UK; jining.sun@hw.ac.uk (J.S.)

Abstract: The ability to predict grinding force for hard and brittle materials is important to optimize and control the grinding process. However, it is a difficult task to establish a comprehensive grinding force model that takes into account of brittle fracture, grinding conditions and random distribution of grinding wheel topography. Therefore, this study developed a new grinding force model for micro-grinding of RB-SiC ceramics. First, the grinding force components and grinding trajectory were analyzed based on the critical depth of rubbing, ploughing and brittle fracture. Afterwards, the corresponding individual grain force were established and the total grinding force was derived through incorporating the single grain force with dynamic cutting grains. Finally, a series of calibration and validation experiments were conducted to obtain the empirical coefficient and verify the accuracy of the model. It was found that ploughing and fracture were the dominate removal modes, which illustrate the force components decomposed is correct. Furthermore, the values predicted according to proposed model are consistent with the experimental data, with the average deviation of 6.793% and 8.926% for the normal and tangential force, respectively. This suggests that the proposed model is acceptable and can be used to simulate the grinding force for RB-SiC ceramics in practical.

Keywords: grinding force model; rubbing; plastic; brittle fracture; protrusion height

1. Introduction

Reaction bonded silicon carbide (RB-SiC) ceramics is a good candidate material for large space optical mirror due to its high strength, high thermal conductivity, enhanced radiation stability and thermal shock resistance characterizes [1-3]. To date, grinding with superhard fine abrasives is the primary method used in achieving the desired tolerances and surfaces integrity for engineering ceramic machining [4,5]. However, inherent high hardness and brittleness presenting a barrier to plastic removal of RB-SiC ceramics. During the grinding process, the interaction between abrasive grains and RB-SiC ceramics leads to unavoidable damages which consist of cracks, voids, dislocations and stacking faults etc. Those damages will affect the service life of the components, especially the brittle fracture is the key factor. To minimize the damages induced by brittle facture, several previous studies have been performed to evaluate

the relationship between grinding force and removal behavior [6-7]. Grinding force is a crucial indicate factor on the grinding quality, which means that whether cracks formed or not is directly controlled by applied normal load in the grinding process. The form accuracy and ground device quality, especially surface and subsurface integrity are strongly influenced by grinding force. Therefore, prediction and proposed controlling method of grinding force is significant for improving the surface and subsurface integrity of ceramics components. Numerous researchers have attempted to modelling the force for surface grinding from theoretical and experimental approaches. Malkin et al [8]. argued that the grinding force should decomposed by two parts, namely, cutting deformation and sliding force. Werner et al [9] presented an empirical model by surperimposing all instantaneous frictional and cutting forces of individual edges in contact with the workpiece. However, Ge et al. [10] suggest that Werner's model not distinguish the sliding and cutting from the physical relationships in grinding, therefore author construct a grinding force model which separated sliding, plowing and cutting force based on the analyses of grinding trajectory and grain workpiece contact. Badger et al [11] developed two methods for calculating grinding force. One is based on Challen and Oxley's 2D slip-line filed model of the contact between grit and workpiece, another is based on Willams and Xie's 3-D model of a three-dimensional asperity which generating a series of grooves on the workpiece. To gain accurate results the grinding wheel profile and some material properties need to be measured. Afterwards, Hecker et al. [12,13] proposed a model for grinding force and power based on the probabilistic distribution of undeformed chip thickness which assumed to be distribute as Rayleigh probability density function. However, most of above mentioned models concerned grinding of metallic materials, in which just involved rubbing, ploughing, chip formation stages. Whereas, brittle fracture is the most significant distinction removal mechanism between ceramics and metallic materials. The adoption of them results in prediction of hard and brittle materials has deviations. This indicates that the transition from ductile deformation to brittle fracture removal mode must be considered when modelling grinding force for ceramics. Therefore, Wu et al. [14] extended Hecker's model and predicted the grinding force for brittle materials considering co-existing of ductility of brittleness. In this model, the surface and subsurface damage was quantitative characterized, but the random distribution of grains height and size was not considered. Nevertheless, based on the random grit distribution which described by stochastic grit density function, Chang and Wang [15] developed a stochastic grinding force. Cheng et al [16] established a predictive grinding force model in micro-slot grinding of single crystal sapphire. Even though different orientation of sapphire was taken into account, the brittle fracture physical characterize was not exhibited in the model. Excepts above mentioned studies, researchers also developed novel grinding forces model of ultrasonic variation assisted grinding for brittle materials such as zirconia [17], alumina [18], and silica glass and Al_2O_3 ceramic [19]. Most of them attempted to build grinding force model according to the analysis of the motion trajectory of grits and material removal mechanism. Despite many models could be used to predict grinding forces, it needs optimization and improvement. In particular, it can found that considering the brittle fracture characterize at the same time combining the random distribution of grinding wheel grains is the major impediment to modeling grinding force for RB-SiC ceramics.

Consequently, in order to obtain a predictive model for ceramics, an improved theoretical force model was proposed in this paper, which taken the random distribution of abrasives, grinding trajectory and different material deformation stage into consideration. The components of grinding force, contact length of grinding wheel and workpiece were analyzed first. Then, the corresponding critical depth of elastic, plastic and brittle fracture stage were calculated. Afterwards, single grain scratch rubbing, ploughing and brittle fracture force was given out based on different interaction mechanisms. During the modelling process, the grain shape, protruding height of diamond grains and random distribution of grinding wheel grains

feature were measured using Alicona microscope and the obtained parameters were used as the input variables. Hence, the total grinding force was obtained by incorporating grains involved in each stage.

2. New grinding force model

The detail structure of developing process of the proposed grinding force model was illustrated in **Figure 1.** The distance between two continuous dynamic active grains, effective radius of the indenter tip and RB-SiC ceramics physic properties were firstly taken as the input parameters to calculate the critical depth transition from elastic to plastic and finally to brittle fracture. Then, based on each stages of critical depth, the total grinding force of RB-SiC ceramics was decomposed into different components and the corresponding stress state under a single grain at each stage was build. In the end, the amount of dynamic active grains participates in cutting, protruding height of diamond grains and random distribution of grains were used to develop the total grinding force model. The novelties of the modelling approach lie in two aspects, i.e. developing the grinding force components including rubbing, ploughing and brittle fracture separately, taking into consideration of the brittle fracture removal mode which is particularly necessary for ceramics. Besides, the random grinding wheel topography was chosen as an input parameter to compute the force.

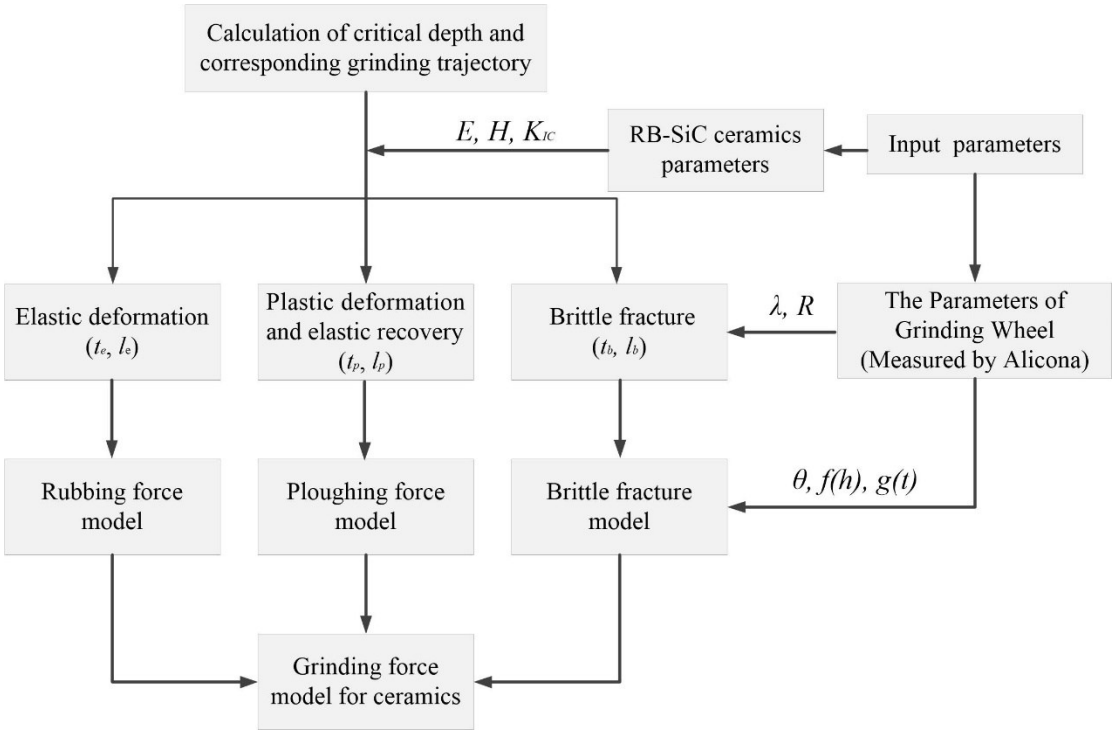

Figure 1. The diagram of developing process of the proposed grinding force model.

During grinding process, the grinding force is fully dependent on the grinding depth. On the basis of the grinding trajectory and material properties, the whole machining process during the interaction between grains and workpiece can be divided into four regimes, namely, elastic, plastic, chip formation and brittle fracture. However, the inherent hardness and brittle characteristics of RB-SiC ceramics result in a little space left for the ductile transition to brittle fracture (DTB). Therefore, the elastic deformation and elastic recovery at the rear of the indenter cannot be ignored in the modeling force, especially at the initial contact of nanoscale grinding. Besides, the calculated minimum depth for chip formation is much larger than the depth for

DTB (**Section 2**). It indicates that the ductile chip formation can be assumed not considered in the force modeling. This phenomenon can be explained by the large negative rake angle of diamond grains and material brittleness. That is to say, the fracture occurred in machining plays an important role at material removal stage. As a result, in according to the critical depth of elastic to plastic transition t_e and ductile to brittle transition tb, the material removal process can be divided into two parts as following:

$$\left.\begin{cases} t < t_e \text{ (rubbing)} \\ t_e < t < t_b \text{ (ploughing)} \end{cases}\right\} \text{(Ductile region)} \qquad \left.\begin{cases} t > t_b \text{ (fracture)} \end{cases}\right\} \text{(Brittle fracture region)} \tag{1}$$

In term of depth of gradient, the predictive model of grinding forces should be made of rubbing force, ploughing force and brittle fracture chipping force. The F_T and F_N force can be expressed by Eqs. (2) and (3):

$$F_N = F_{ne} + F_{np} + F_{nb} \tag{2}$$

$$F_T = F_{te} + F_{tp} + F_{tb} \tag{3}$$

Where F_{ne}, F_{np}, F_{nb} are the normal rubbing and ploughing force and fracture chip force, F_{te}, F_{tp}, F_{tb} are the tangential sliding and ploughing force and fracture chipping force.

2.1 Trajectory length of single diamond grain-workpiece

Based on previous discussion on the different stages, the geometrical contact arc length between the workpiece and grinding wheel is indicated by:

$$l_t = l_e + l_p + l_b \tag{4}$$

Where l_t is the ideal contact length equal to $l_t = \sqrt{ad_s}$ in which the motion and deformation of grinding wheels and workpiece are neglected, a_p is the grinding depth, d_s is the diameter of the grinding wheel., l_e, l_p and l_b are the contact length in elastic, plastic and brittle fracture stages, respectively. As shown in **Figure 2**, from the proportional relationships it can be deduced:

$$l_e = \frac{t_e}{t_m} l_t \tag{5}$$

$$l_p = \frac{l_t}{t_m}(t_b - t_e) \tag{6}$$

$$l_b = l_t - l_e - l_p \tag{7}$$

Where t_m is the maximum undeformed chip thickness.

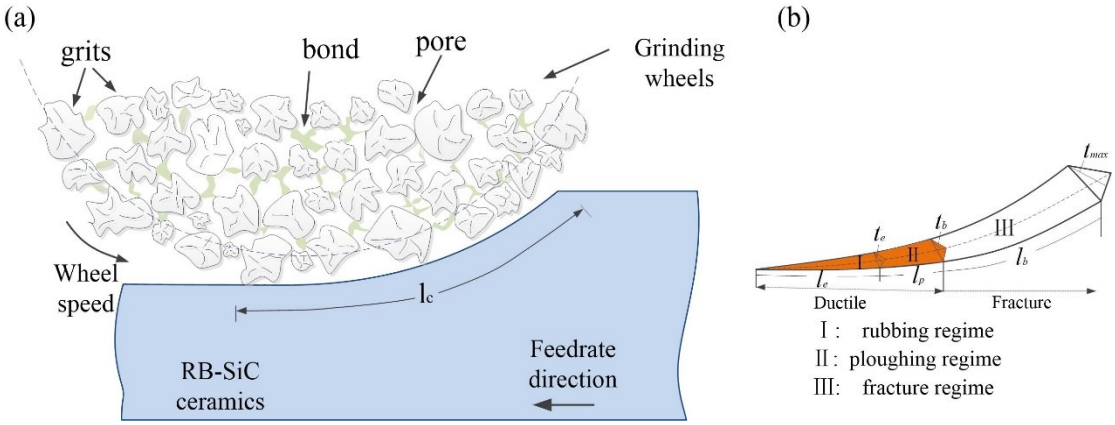

Figure 2. (a) The schematic diagram of grinding process; (b) three stages divided in a whole contact trajectory.

2.2 Dynamic grinding trajectory and uncut chip thickness

2.2.1 The critical depth for elastic to plastic transition

The parameters of critical depth for each stages should be estimated first. For the elastic to plastic transition the maximum contact stress P_{max} at critical place can be obtained by [20]:

$$P_{max} = \frac{2E_r a_p}{\pi R} \approx 1.6\frac{H}{2.8} \tag{8}$$

Then, the critical depth calculated based on hertz theory is expressed by [21]:

$$t_e = 0.428a_p = \frac{P_{max}\pi R}{2E_r} = 0.1223\frac{\pi HR}{E_r} \tag{9}$$

where, E_r is the composite elastic modulus, a_p is the indentation depth induced by P_{max} and R is the effective radius of the indenter tip, which can be calculated by the following equation:

$$E_r = (\frac{1-\upsilon_1^2}{E_1} + \frac{1-\upsilon_2^2}{E_2})^{-1} \tag{10}$$

Where, E_1 and E_2 is the elastic modulus of workpiece and diamond indenter, respectively. υ_1 and υ_2 is Poisson's ratio of the workpiece and diamond indenter, respectively.

2.2.2 The critical depth of cut for chip formation

The minimize depth of cut for chip formation thickness t_{cr} can be determined by the formula proposed by [22]:

$$t_{cr} = R[1-\cos(\pi/4-\beta/2)] \tag{11}$$

Where β is the friction angle that equal to arctan(μ), μ is the apparent friction coefficient that can be get from our previous study [23].

2.2.3 The critical depth for ductile to brittle transition

If assumed the effect of grinding parameters on material properties is ignored, the critical transition from ductile to brittle fracture can be determined by the material elastic modulus E_1, hardness H_1 and fracture toughness K_{IC}. The depth of DTB can be predicted by the following equation [4]:

$$t_b = \varepsilon(\frac{E_1}{H_1})(\frac{K_{IC}}{H_1})^2 \tag{12}$$

Where ε is a constant as 0.15. Through the comparison, it can be found that the critical depth for chip formation (t_{cr}=147.43 nm) is much larger than DTB (t_b=36.83 nm) depth. For this reason, the ductile chip formation force can be ignored in this model.

2.2.4 The maximum undeformed chip thickness in micro-grinding

According to the grinding principle, for two continuous cutting grains the maximum underformed chip thickness t_{max} could be expressed by [24]:

$$t_{max} = (2\lambda \frac{v_w}{v_s} \sqrt{\frac{a}{d_s}})^{\frac{1}{2}} \quad (13)$$

Where λ is the space between the dynamic active cutting grains, d_s is the diameter of the grinding wheel, v_w is the feed rate and v_s is the peripheral speed of the grinding wheel. From kinematic trajectory and simplify considerations, it can be assumed that the active continuous cutting grains are at the same protrusion height. So the space between the continuous cutting grains can be get from the profile of grinding wheel topography as depicted in **Section 3**.

2.3 Normal and tangential force per single grain

2.3.1 Cutting force in elastic stage

Figure 2a shows the schematic diagram of contact region between the grain and workpiece. The workpiece surface will undergoing elastic deformation at the initial stage due to small grinding depth. At such depth, the grain tip can be regarded as a sphere contacting with the workpiece surface (illustrated in **Figure 5**). Based on Hertz theory [21], the normal force and tangential force can be derived from Eqs. (13) and (14):

$$F_{ne} = \frac{4}{3} E_r R^{1/2} t^{3/2} \quad (14)$$

$$F_{te} = \mu_a \frac{4}{3} E_r R^{1/2} t^{3/2} \quad (15)$$

Where, μ_a is the adhesion fraction coefficient [23].

2.3.2 Cutting force in plastic stage

As the grinding depth increased, the workpice will start to deform plastically at the point where the yield criterion is satisfied. While, the normal and tangential ploughing force can be obtained as follows:

$$dF = \sigma_y dA \quad (16)$$

Where σ_y is the compressive yield stress at contact area [25]:

$$\sigma_y = (H^4 / E)^{1/3} \quad (17)$$

The contact projected area in the normal direction A and thrust direction S can be given by:

$$A = \pi(2Rt - t^2)/2 \quad (18)$$

$$S = R^2 \cos^{-1}(\frac{R-t}{R}) - (R-t)\sqrt{2Rt - t^2} \quad (19)$$

Thus, the normal and thrust force (plastic stage) can be obtained by submit Eq. (17), Eqs. (18) and (19) into Eq. (16):

$$F_{np} = \frac{\pi\sigma_y(2Rt - t^2)}{2} = \frac{\pi(H^4 / E)^{1/3}(2Rt - t^2)}{2} \quad (20)$$

$$F_{tp} = (H^4 / E)^{1/3}(R^2 \cos^{-1}(\frac{R-t}{R}) - (R-t)\sqrt{2Rt - t^2}) \quad (21)$$

2.3.3 The elastic recovery force at the rear of the tool in the plastic deformation region

The grinding force caused by the elastic recovery of the material at the rear of the tool cannot be neglected. The spring back height of the newly machined surface can be estimated by [26]:

$$t_s = \chi R \frac{H}{E} \tag{22}$$

Where χ is a scaling constant for the best fit.

As the material is assumed to give a perfect elastic plastic response, the plastic depth results only the plastic flow around the tip. Hence, the stress on the flank face is equal to σy. The elastic deformation caused tangential force can be defined by:

$$F_{en} = \sigma_f A_e = \chi \pi \sigma_f R^2 H \frac{1}{E}(1 - K_2 \frac{H}{2E}) \tag{23}$$

$$F_{et} = \mu_a \chi \pi \sigma_f R^2 H \frac{1}{E}(1 - K_2 \frac{H}{2E}) \tag{24}$$

2.3.4 Contact force in the brittle zone

While at last stage $t > t_b$, material would be primarily removed in the brittle fracture mode. In this regime, the generation and propagation of cracks are the main reason of facture chipping. As shown in **Figure 3**, median cracks will form and propagate first beneath the grits with the increase of normal load. At the following unloading process, the lateral crack will be generation due to mismatch of residual stress between the interface of elastic and plastic zone. Afterwards, the chipping will generate and the materials will be removed. The depth C_h and length C_l of the lateral crack can be obtained by the following equations [27]:

$$C_l = C_2 (\frac{1}{\tan\theta})^{5/12} [\frac{E^{3/4}}{HK_{IC}(1-v^2)^{1/2}}]^{1/2} (F_{nb})^{5/8} \tag{25}$$

$$C_h = C_2 (\frac{1}{\tan\theta})^{1/3} \frac{E^{1/2}}{H} (F_{nb})^{1/2} \tag{26}$$

Where θ is the half apex angle of the indenter, C_2 is a dimensionless constant, which is independent of material-indenter system, and C_2=0.226 [23].

Moreover, the plastic deformation zone depicted in **Figure 3** is approximated by a semicircle of radius b [28]. The plastic zone radius is expressed as a function of not only the load and material properties, but also of the grits geometry. An empirical relationship between yield strength σ_y and elastic modulus, poisson ratio is used to obtain the plastic zone radius.

$$b = \left(\frac{3(1-2\nu)}{5-4\nu} + \frac{2\sqrt{3}}{\pi(5-4\nu)} \frac{E}{\sigma_y} \cot\theta \right)^{\frac{1}{2}} a \tag{27}$$

Where $a = t\tan\theta$, as described above the lateral cracks initiated at the bottom of plastic deformation zone, therefore the depth b can be assumed equal to C_h. So combining the Eq. (23) and Eq. (24), the final force in brittle fracture regime can be written as:

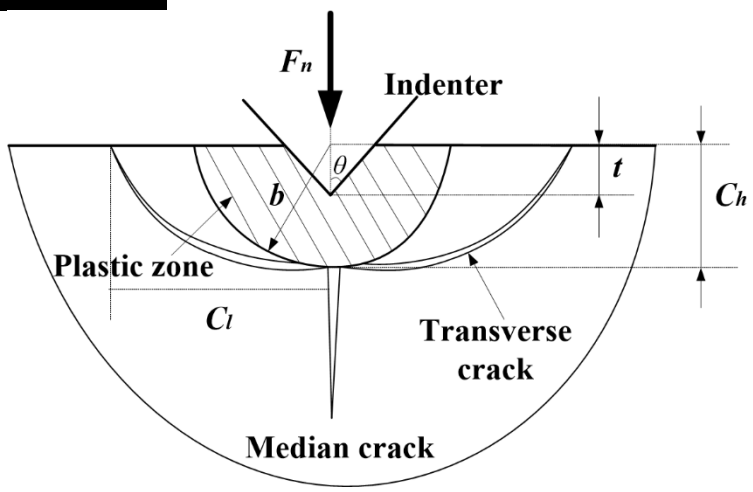

Figure 3. Illustration of material removal volume in brittle region during grinding.

$$F_{nb} = Ct^2H^2(\tan\theta)^{8/3}\left(\frac{3(1-2\upsilon)}{E(5-4\upsilon)} + \frac{2\sqrt{3}}{\pi(5-4\upsilon)}\frac{1}{\sigma_y}\cot\theta\right) \quad (28)$$

$$F_{tb} = Ct^2H^2(\tan\theta)^{8/3}\frac{C_l}{C_h}\left(\frac{3(1-2\upsilon)}{E(5-4\upsilon)} + \frac{2\sqrt{3}}{\pi(5-4\upsilon)}\frac{1}{\sigma_y}\cot\theta\right) \quad (29)$$

where $C=1/C_2$. Thus, F_{nb} and F_{tb} can be calculated from the above Eq. (28) and Eq. (29), respectively.

2.4 Measurement of the grinding wheel by Alicona

2.4.1 The topography of grinding wheel surface

To characterize the cutting area surface, the 3D topography data of grinding wheel was measured by Alicona directly. The surface digitization is based on Focus-Variation. The resolution of minimum vertical repeatability is less than 0.12 nm. The data coexistence of longitudinal, lateral and height of wheel topography are necessary for identify the diamond grains distribution and dimensions. **Figure 4** shows the topography of the #6000 resin bond and 100% grain density grinding wheel which was measured using 50× objective.

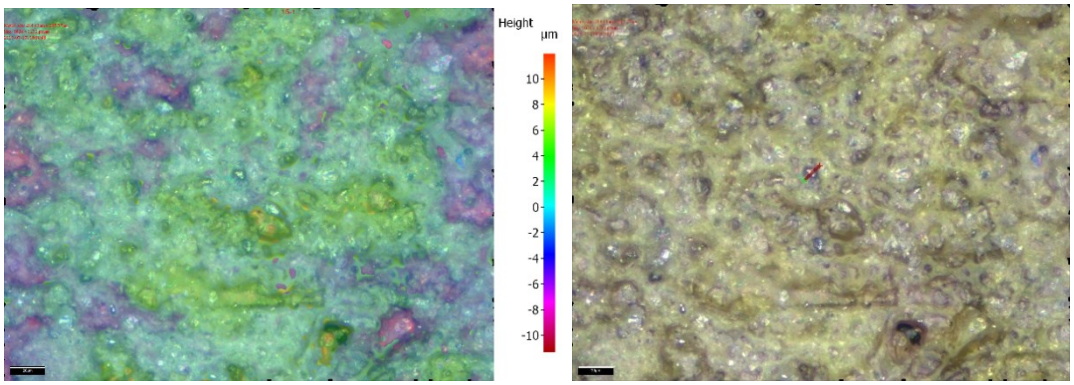

Figure 4. The 3D topography of #6000 grinding wheel.

2.4.2 The parameters of cutting edge radius and cone angle

Each digitized image is processed to extract the wheel surface information in the context of average cutting edge diameter, average cutting edge angle, average space between the dynamic active grains, and corresponding static density as a function of the radial distance into the wheel. **Figure 5a** shows the typical cross section profile of single grain which chosen from **Figure 4b**. As shown in **Figure 5b**, the grain can be simplified as a cone shape with sphere tip. The dimension of the tips was fitted using Matlab software with the method of least squares. **Figure 6** shows the averaged value of cutting edge radius and cone angle that obtained by analyzing a population of grains.

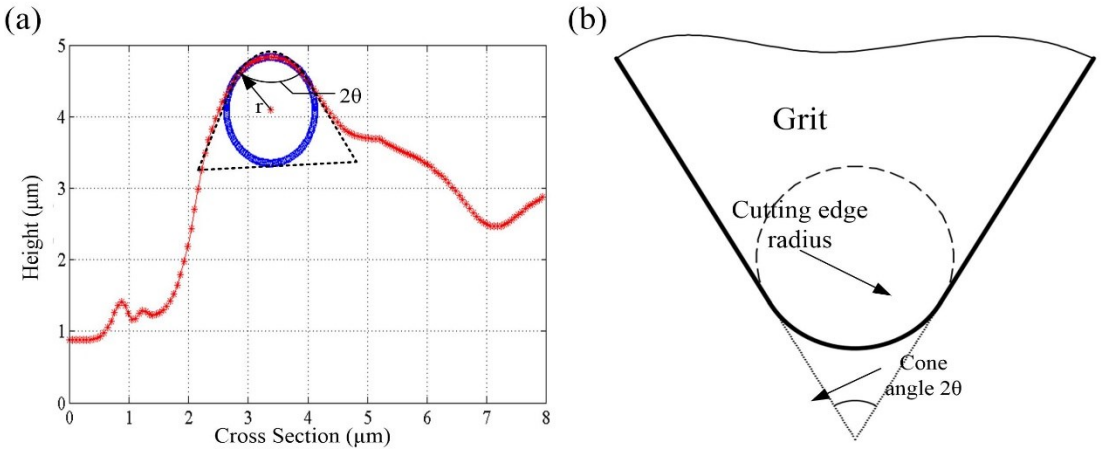

Figure 5. (a) Typical cross sectional profile of grain and (b) the simplified model of grain.

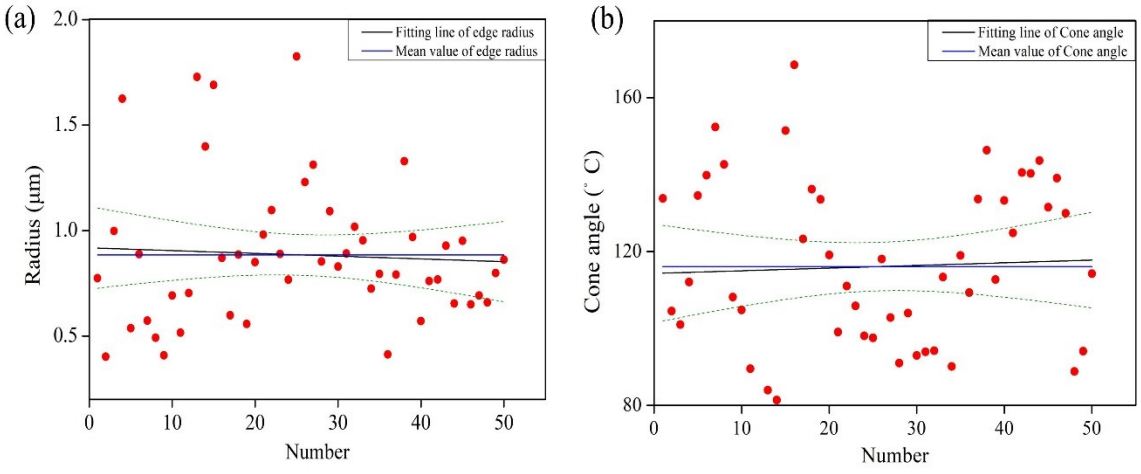

Figure 6. The measured data of grains radius (a) and cutting cone angle (b).

2.4.3 Determination of active grains protrusion height and number in each stages

Figure 7 shows the cross sectional profile along the periphery of grinding wheel. Owing to the interaction between grains, not all of the grains would participate in the cutting stage. Malkin [29] proposed that the grains and cutting edges can be evaluated through setting the threshold value. For simplify considerations, it will be assumed that the active continuous cutting grains are at the same protrusion height as depicted in **Figure 7**.

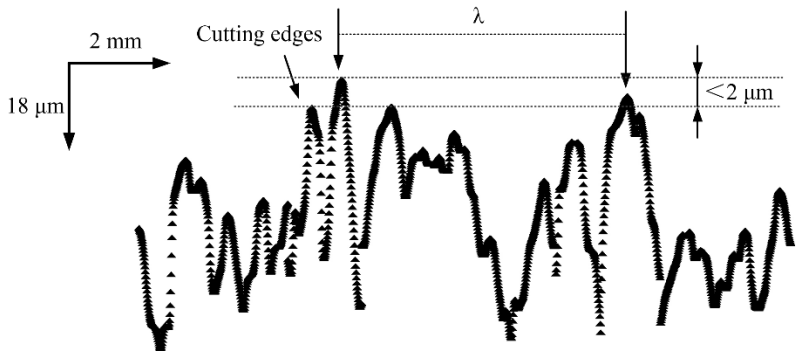

Figure 7. The traced profile along the periphery of grinding wheel.

Figure 8 illustrates the details of grain protrusion height on the grinding wheel surface, which distribute in the form of normal distribution. The Gaussian function was applied to fit the data as following expression:

$$f(h) = \frac{1}{\sqrt{2\pi}\cdot\sigma} e^{-\frac{(h-\delta)^2}{2\sigma^2}} \tag{30}$$

where, σ is the standard deviation and δ is the mean value of grain protrusion height.

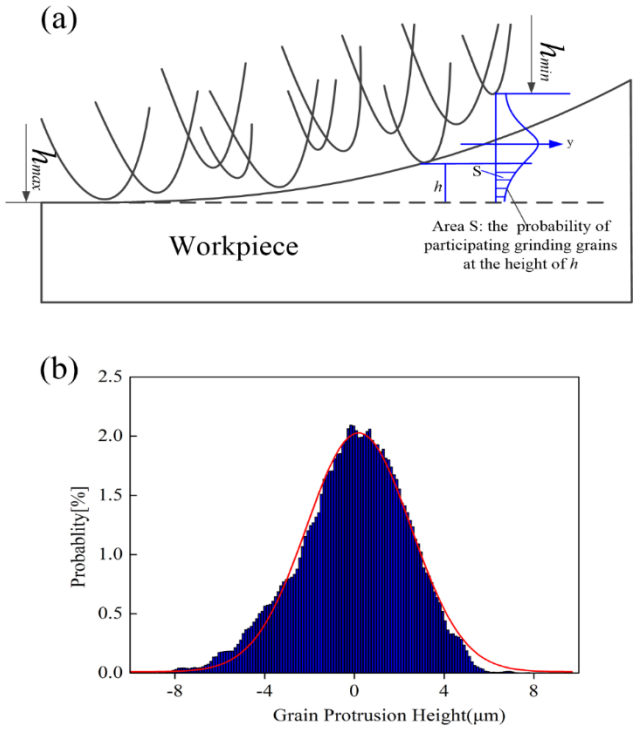

Figure 8. (a) Schematic of the grain size distribution showing maximum and minimum protrusion height of the grain and the probability distribution of other sizes of the grains, (b) Normal distribution plot of the frequency verse the grain protrusion height.

The active grains number in each segment can be determined by:

$$\Delta N = N_a \cdot l_{total} \cdot w \cdot \int_{h_{max}}^{\Delta h} f(h)dh \tag{31}$$

Where, N_a is the average number of grains per units area, h_{max} is the value of highest grain protrusion, w is the contact width of grinding and Δh is the difference value between h_{max} and the corresponding height in each stages.

Besides, N_a can be approximately estimated from [30]:

$$N_a = \frac{100}{d^2} \times (\varphi(D))^{\frac{2}{3}} \tag{32}$$

Where d and $\varphi(D)$ are the average diameter and volume fraction of diamond grain.

2.5 Superposition of single grain grinding forces

As shown in **Figure 8b** the cutting depth has relationship with grain protrusion height, the cutting depth probability density can be describe as:

$$g(t) = -\frac{1}{\sqrt{2\pi}\sigma} e^{-\frac{(h_{\max}-t-\delta)^2}{2\sigma^2}} \quad (0 < t < 10\mu m) \tag{33}$$

By integrating of the tangential and normal force model per grain in different stage, the total tangential and normal force at each stage can be expressed as:

First stage, $0 < t < t_e$

$$F_n = \Delta N \cdot E(F_{ne}) = \Delta N \int_0^{t_m} F_{ne} g(t) dt = N_a l_t w \int_{h_m - t_m}^{h_m} \int_0^{t_m} F_{ne} g(t) f(h) dt dh \tag{34}$$

$$F_t = \Delta N \cdot E(F_{te}) = \Delta N \int_0^{t_m} F_{te} g(t) dt = N_a l_t w \int_{h_m - t_m}^{h_m} \int_0^{t_m} F_{te} g(t) f(h) dt dh \tag{35}$$

Second stage, $t_e < t < t_b$

$$\begin{aligned} F_n &= \Delta N_1 \cdot E(F_{ne}) + \Delta N_2 \cdot E(F_{np}) + \Delta N_2 \cdot E(F_{en}) \\ &= N_a l_t w \left(\int_{h_m - (t_m - t_e)}^{h_m} \int_0^{t_m - t_e} F_{np} g(t) f(h) dt dh + \int_{h_m - t_m}^{h_m - (t_m - t_e)} \int_{t_m - t_e}^{t_m} F_{ne} g(t) f(h) dt dh + F_{en} \int_{h_m - (t_m - t_e)}^{h_m} f(h) dh \right) \end{aligned} \tag{36}$$

$$\begin{aligned} F_t &= \Delta N_1 \cdot E(F_{te}) + \Delta N_2 \cdot E(F_{tp}) + \Delta N_2 \cdot E(F_{et}) \\ &= N_a l_t w \left(\int_{h_m - (t_m - t_e)}^{h_m} \int_0^{t_m - t_e} F_{tp} g(t) f(h) dt dh + \int_{h_m - t_m}^{h_m - (t_m - t_e)} \int_{t_m - t_e}^{t_m} F_{te} g(t) f(h) dt dh + F_{et} \int_{h_m - (t_m - t_e)}^{h_m} f(h) dh \right) \end{aligned} \tag{37}$$

The third stage, $t > t_b$

$$\begin{aligned} F_n &= \Delta N_1 \cdot E(F_{nb}) + \Delta N_2 \cdot E(F_{np}) + \Delta N_3 \cdot E(F_{ne}) \\ &= N_a l_t w \left(\int_{h_m - (t_m - t_b)}^{h_m} \int_0^{t_m - t_b} F_{nb} g(t) f(h) dt dh + \int_{h_m - (t_m - t_e)}^{h_m - (t_m - t_b)} \int_{t_m - t_b}^{t_m - t_e} F_{np} g(t) f(h) dt dh + \int_{h_m - t_m}^{h_m - (t_m - t_e)} \int_{t_m - t_e}^{t_m} F_{ne} g(t) f(h) dt dh \right. \\ &\left. + F_{en} \int_{h_m - (t_m - t_e)}^{h_m - (t_m - t_b)} f(h) dh \right) \end{aligned} \tag{38}$$

$$\begin{aligned} F_t &= \Delta N_1 \cdot E(F_{tb}) + \Delta N_2 \cdot E(F_{ts}) + \Delta N_3 \cdot E(F_{te}) \\ &= N_a l_t w \left(\int_{h_m - (t_m - t_b)}^{h_m} \int_0^{t_m - t_b} F_{tb} g(t) f(h) dt dh + \int_{h_m - (t_m - t_e)}^{h_m - (t_m - t_b)} \int_{t_m - t_b}^{t_m - t_e} F_{tp} g(t) f(h) dt dh + \int_{h_m - t_m}^{h_m - (t_m - t_e)} \int_{t_m - t_e}^{t_m} F_{te} g(t) f(h) dt dh \right. \\ &\left. + F_{et} \int_{h_m - (t_m - t_e)}^{h_m - (t_m - t_b)} f(h) dh \right) \end{aligned} \tag{39}$$

However, the force model developed above is based on theoretical analyze, which neglect the effects of grinding thermal, cutting depth error caused by stiffness of machine, and imperfect grain geometry. Therefore, three empirical constant K_1, K_2, K_3 should be added to modify the force error produced in rubbing, plastic and brittle fracture stages.

3. Experimental setup and procedure for model validation

To determine the experimental coefficients and verify the force prediction model presented in this work, grinding experiments were carried out on a hybrid ultra-precision micromachine (Micro-3D) under dry cutting. The experiment set up is shown in **Figure 9a**. During grinding process, the grinding forces are measured by a 3-component piezoelectric dynamometer Kistler 9129 AA. Each set of grinding parameters was repeated thrice and the average of three measured value was taken as the final results.

The material tested in present study is RB-SiC ceramics (supplied by Goodfellow Cambridge Ltd. (UK)), which mainly consist of 90% of SiC phase with diameter of 10 μm and nearly 10% of Si phase (as shown **Figure 9b**). **Table 1** listed some typical material properties of RB-SiC ceramics. The workpieces with dimensions of 12.5×12.5×5 mm are clamped on the worktable (**Figure 9a**). A resin bonded diamond grinding wheel with mesh number of #6000 (grit size of 15 μm), diamond concentration of 100%, diameter 6 mm and width 8 mm was used. The grinding wheel was trued using an oilstone stick. The grinding wheel truing conditions are under a wheel speed of 2 m/s, the depth of cut 2 μm, and the transverse feed rate of 0.5 mm/s. In the tests, the grinding speed, feed rate and depth of cut were considered as machining parameters. Experimental parameters for determining coefficient and model calibration, verifying model are given in **Table 2** and **3**, respectively. To study the material removal characteristics and the influence of the RB-SiC microstructures, the machined surface topography was measured by an SEM (Dual beam FEI Helios Nanolab 600i).

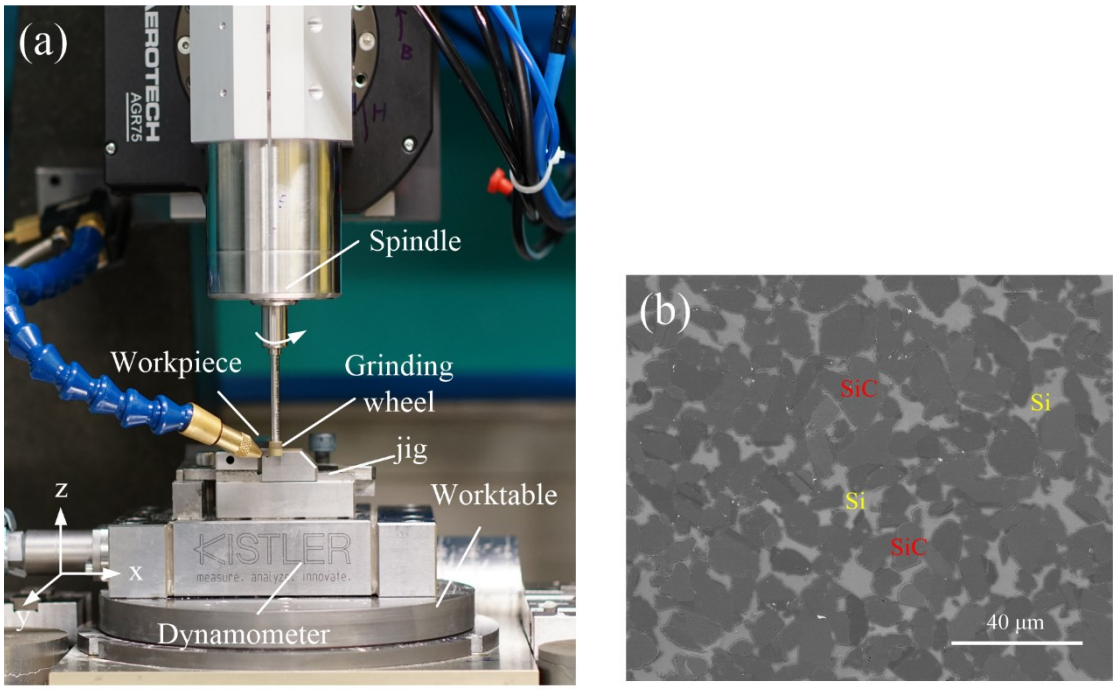

Figure 9. Experiment setup used to validate the proposed model of grinding forces (a) and (b) SEM image of surface morphology of the polished specimen.

Table 1. Workpiece material properties

Workpiece	RB-SiC
Elastic modulus (Gpa)	390
Vickers hardness (Kgf·mm^{-2})	3000
Compressive strength (Mpa)	2000

Fracture toughness KIC (Mpa·m$^{1/2}$)	4.0
Thermal Expansion Coeff. ×10^{-6}/°C	3
Thermal Shock Resistance °C	400
Density ϱ (g/cm^3)	3.1

342 **Table 2.** Grinding parameters for determining coefficient

Exp. No.	Grinding Depth a_e (μm)	Grinding speed n_s (m/s)	Feed rate v_w (mm/s)
1	2	6000	1
2	5	10000	5
3	10	15000	8
4	15	20000	10
5	15	20000	12

343 **Table 3.** Model calibration between predictive and Experiment results

Exp. No.	Grinding Depth a_e (μm)	Grinding speed v_s (m/s)	Feed rate v_w (mm/s)
1	2		
2	5		
3	10	6000	2
4	15		
5		6000	
6	5	10000	5
7		15000	
8		20000	
9			2
10	5	15000	10
11			15
12			20

344 ## 4. Results and Discussion

345 *4.1 The topography of grinding RB-SiC*

346 Surface topography is one of the most important requirements in many engineering
347 applications, as it is considered an important index of product quality. **Figure 10** shows the
348 typical SEM micrographs of ground surface morphology which obtained with the increase of
349 grinding t_{max}. It can be observed that three typical areas: (1) micro-fracture area (2) ductile area
350 (induced by ploughing stripes) (3) macro-fracture area are generated on the machined
351 topography. But there are no obvious ductile debris particles appeared. Besides, the surface
352 integrity obtained with relative small t_{max} (**Figure 8a**) appears to be better than that shown in
353 **Figure 8b** and **c**. This illustrated that brittle fracture become the primary removal mode
354 gradually with the increase of t_{max}. Therefore, it is reasonable to believe that the material
355 removal stages that divided in **Section 2** is suitable.

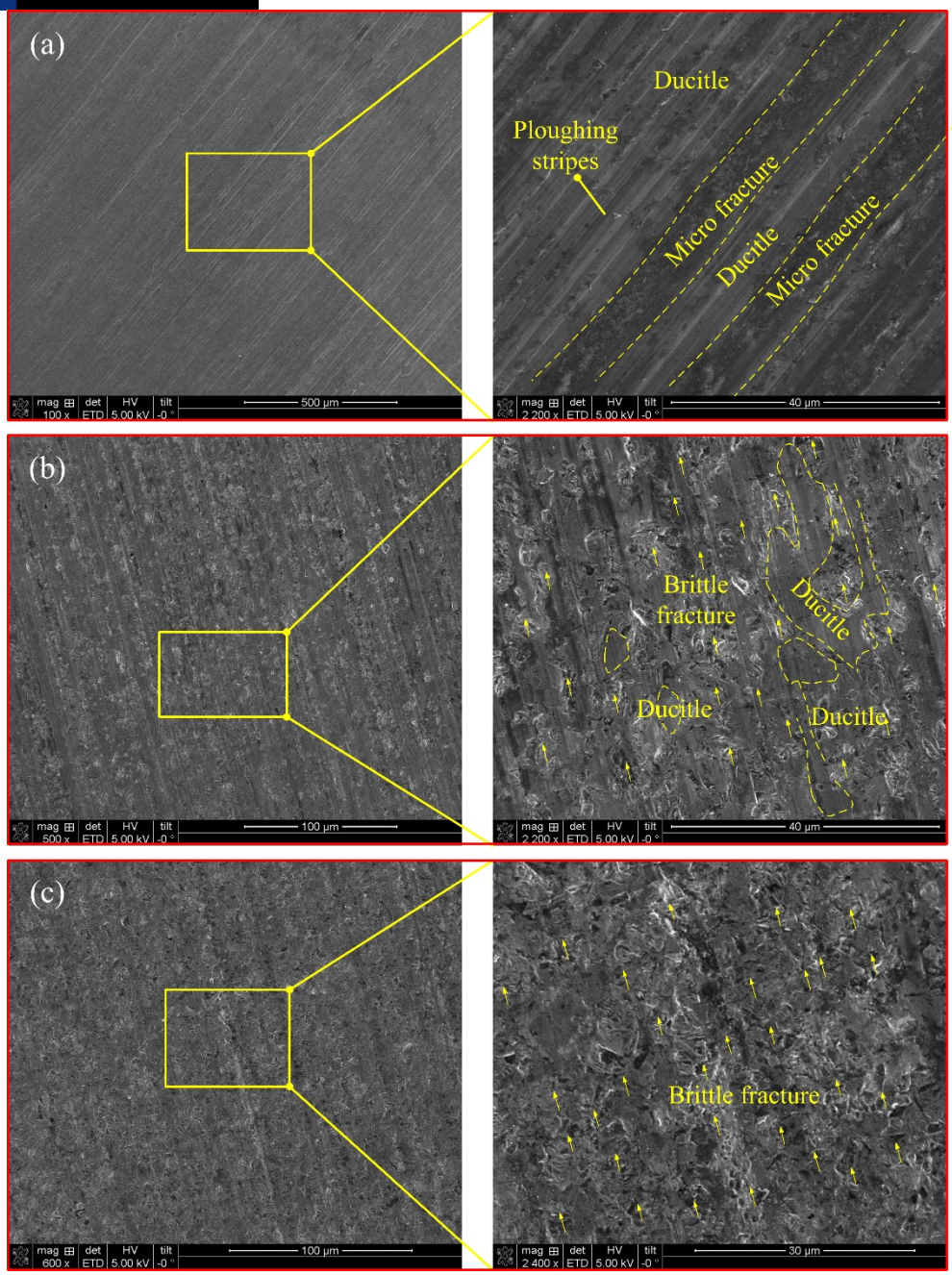

Figure 10. Comparison of the grinding surface morphology with increased t_{max} (a) n_s=6000 r/min, a_e=2 μm, v_w=1 mm/s (b) n_s=15000 r/min, a_e=10 μm, v_w=8 mm/s (c) n_s=20000 r/min, a_e=20 μm, v_w=12 mm/s.

4.2 Determination of Experimental Coefficients

The grinding force can be measured through experiments, then the value of unknown empirical constant K_1, K_2, K_3, χ can be determined through the least square estimation method. **Table 1** list the machining parameters of five group experiments for calibration of the force model. To minimize errors induced by random wheel topography, three runs of each calculation are performed and mean values are illustrated in **Figure 11**. Through the calculation, the parameters are of K_1, K_2, K_3, χ are equal to 0.1228, 8.9934, 0.4116 and 0.1282 respectively. Then, combining the coefficient with Eqs. (34) - (39), the complete theoretical force model can be used to predict the grinding force in practical.

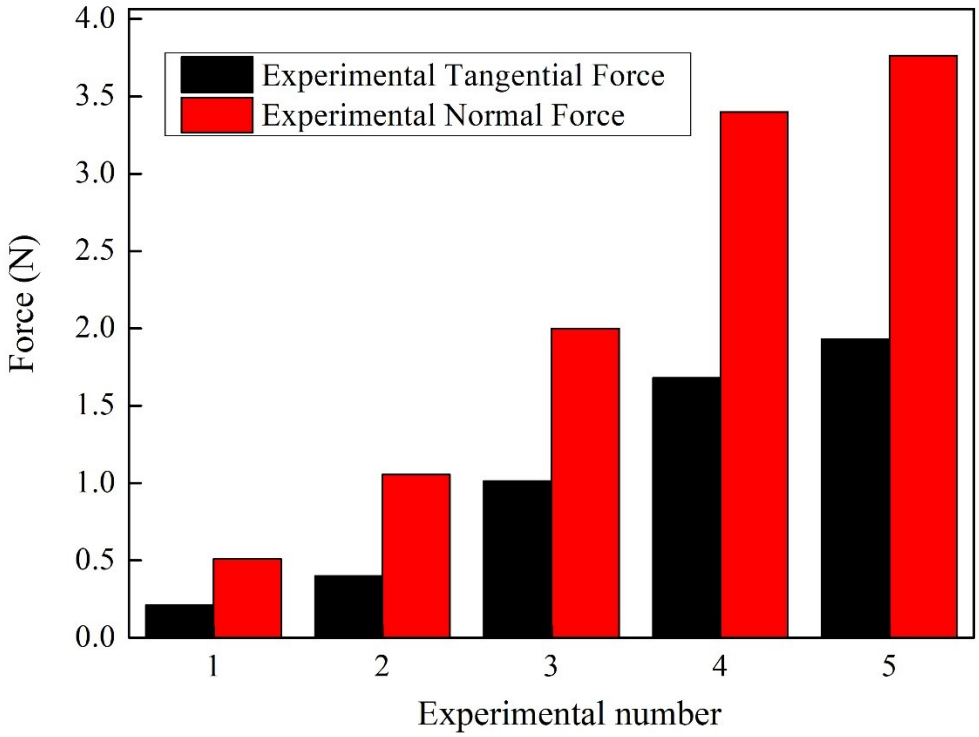

Figure 11. The experimental results of normal and tangential force used for calibration.

4.3 Force model calibration and verification

To validate the grinding force model proposed in this paper, another 12 groups of experiments with varied grinding depth, grinding speed and feed rate were performed. The machining parameters for verifying model was shown in **Table 4**. The predictions of tangential and normal micro-grinding force to RB-SiC ceramics are calculated using the proposed models Eq. (38) and Eq. (39). The comparison results for normal and tangential forces are presented in **Figure 12**. It could be find that the prediction values are consistent with the experimental results. The average percentage of the deviation in normal force and tangential force are 6.793% and 8.926%, respectively. Meanwhile, it can be seen that as grinding depth increased, the tangential and normal grinding force increased with linear relationship. However, both of tangential and normal force decreased with the increase of grinding wheel speed due to the ΔN and the corresponding t_{max} change slightly. The grinding wheel speed will result in reverse effect on the maximum cutting depth. Therefore, the grinding force shows a downward trend with the increasing grinding wheel speed. Besides, it should be note that within the chosen parameter of feed rate, the grinding force exhibits a significant upward trend and non-linear proportional to feed rate. In this process, the increased t_{max} lead more material removal volume in brittle region and the corresponding brittle grinding force increased intensely.

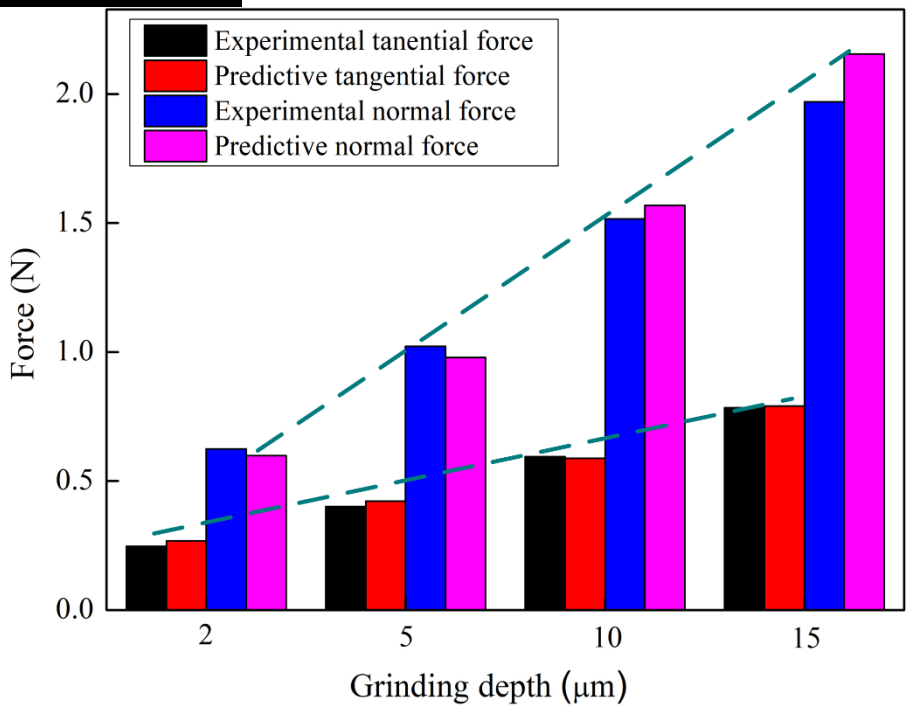
Experimental tanential force
Predictive tangential force
Experimental normal force
Predictive normal force
Force (N)
0.0
0.5
1.0
1.5
2.0
2
5
10
15
Grinding depth (μm)

388

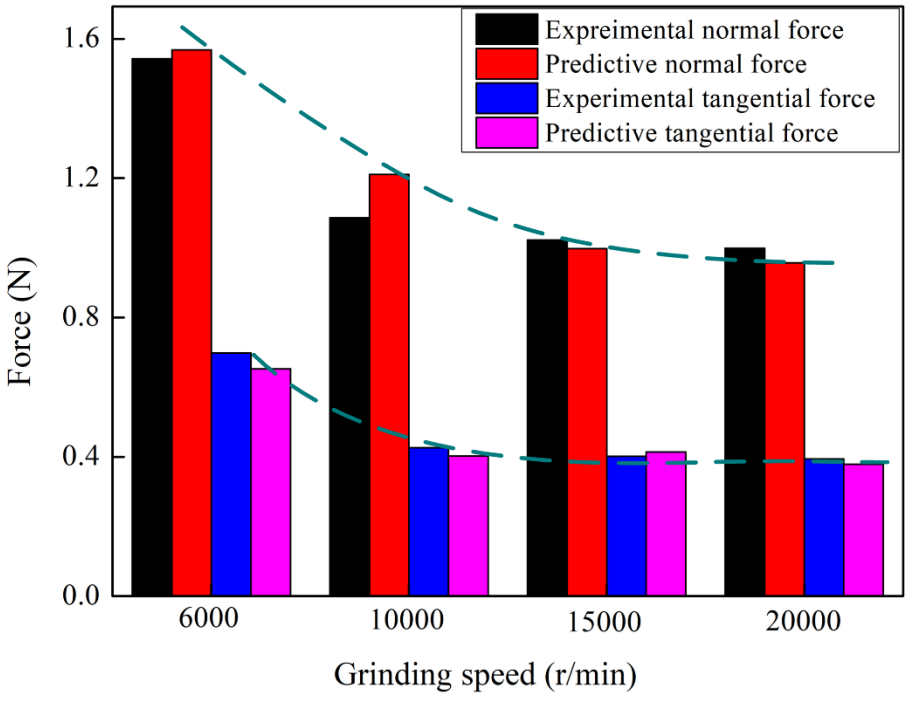
Expreimental normal force
Predictive normal force
Experimental tangential force
Predictive tangential force
Force (N)
0.0
0.4
0.8
1.2
1.6
6000
10000
15000
20000
Grinding speed (r/min)

389

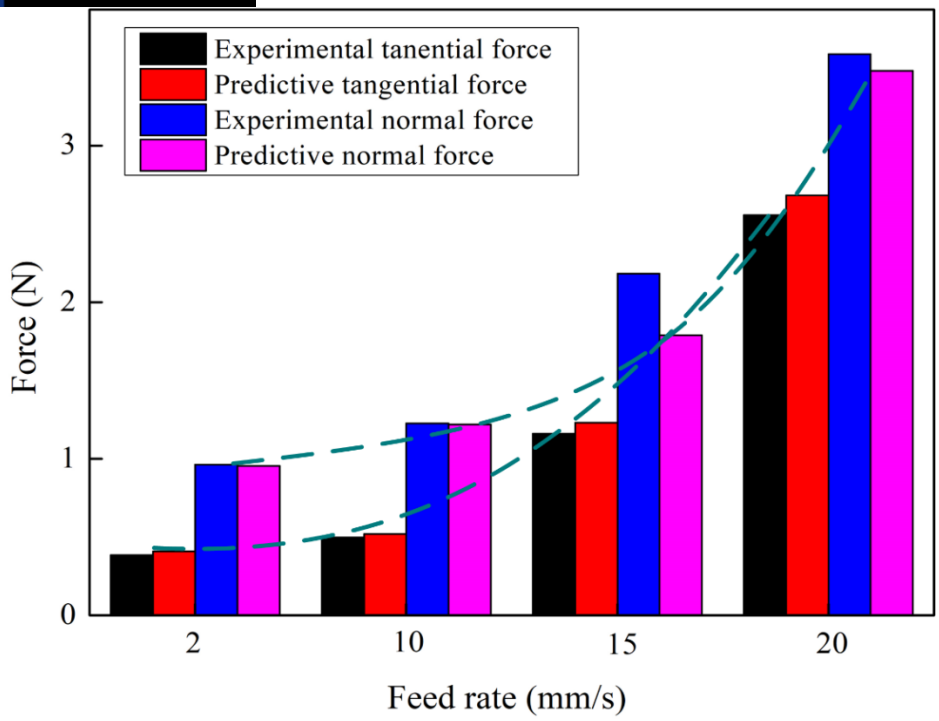

Figure 12. The experimental results for assessing the accuracy of proposed model.

5. Conclusions

A theoretical grinding force model for RB-SiC ceramics has been established with the consideration of rubbing, plastic flow and brittle fracture removal mechanism. What's more, the parameters of the grains random distribution and protrusion that measured with the aid of Alicona were fed back into the model to integrating individual grain force. Accurate calibration experiments were conducted to obtain empirical coefficients under different grinding parameters. The validity of the model is proved by comparing the experimental data with the predicted values.

1) The grinding wheel topography measurement results suggest that the height of grain protrusion distribution obeys normal distribution law.
2) The SEM observations of grinding surface topography indicated that ploughing and brittle fracture were the dominate deformation mechanism. Meanwhile, no ductile chips were found within the chosen grinding parameters. These phenomena revealed that the assumed grinding force components including rubbing, ploughing and brittle fracture is feasibility.
3) The feed rate has the most significant impacts on the grinding force, and the grinding force is proportional to feed rate and grinding depth. In contrast, increasing of grinding wheel speeds will result in a downward trend of the grinding force.
4) The validation experimental results show that the predicted grinding force model can be employed to simulate the grinding forces. The average percentage of deviation of normal force and tangential force are 6.793% and 8.926%, respectively. Therefore, the proposed methodology was proven to be able capture actual grinding process of ceramics.

6. Acknowledgements

The authors would like to thank the financial from the Major State Basic Research Development Program of China (973 Program, Grant No. 2011CB013202), National Key

Research and Development Program of China (2016YFB1102204) and the EPSRC project (EP/K018345/1) in the UK for this study.

Reference

[1] Ebizuka, N.; Dai, Y.; Eto, H.; Lin, W.; Ebisuzaki, T.; Omori, H.; Handa, T.; Takami, H.; Takahashi, Y. Development of SiC ultra-light mirror for large space telescope and for extremely huge ground-based telescope. Proc. SPIE. 2003, 4842, 329-334.

[2] Zhou, H.; Zhang, C.; Cao, Zhou, X. Lightweight C/SiC mirrors for space application. Proc. SPIE. 2006, 6148, 61480L-1.

[3] Kasuga, H.; Ohmori, H.; Mishima, T.; Watanabe, Y.; Lin, W. Investigation on mirror surface grinding characteristics of SiC materials. J. Ceram. Process. Res. 2009, 10, 351–354.

[4] Bifano, T.G.; Dow, T.A.; Scattergood, R.O. Ductile-Regime Grinding: A New Technology for Machining Brittle Materials, J. Eng. Ind. 1991, 113, 184-189.

[5] H.H.K. Xu, S. Jahanmir, L.K. Ives, Material removal and damage formation mechanisms in grinding silicon nitride, J. Mater. Res. 1996, 11, 1717–1724.

[6] Liu, W.; Deng, Z.; Shang, Y.; Wan, L. Effects of grinding parameters on surface quality in silicon nitride grinding, Ceram. Int. 2017, 43, 1571–1577.

[7] Li, B.; Ni, J.; Yang, J.; Liang, S.Y. Study on high-speed grinding mechanisms for quality and process efficiency, Int. J. Adv. Manuf. Technol. 2014, 70, 813–819.

[8] Malkin S.; Guo, C. Grinding technology: theory and applications of machining with abrasives, 2nd edn; Industrial Press, New York, 2008.

[9] Werner G. Influence of work material on grinding forces. CIRP Ann-Manuf Techn.1978, 27, 243–248.

[10] Wang, D.; Ge, P.; Bi, W.; Jiang, J. Grain trajectory and grain workpiece contact analyses for modeling of grinding force and energy partition, Int. J. Adv. Manuf. Technol. 2014, 70, 2111–2123.

[11] Badger, J.A.; Torrance, A.A. Comparison of two models to predict grinding forces from wheel surface topography, Int. J. Mach. Tools Manuf. 2000, 40, 1099–1120.

[12] Hecker, R.L.; Liang, S.Y.; Wu, X.J.; Xia, P.; Jin, D.G.W. Grinding force and power modeling based on chip thickness analysis, Int. J. Adv. Manuf. Technol. 2007, 33, 449–459.

[13] Hecker, R.L.; Nacional, U;. Pampa, D. La. Analysis of Wheel Topography and Grit Force for Grinding Process Modeling, 2003, 5, 13–23.

[14] Wu, C.; Li, B.; Yang, J.; Liang, S.Y. Prediction of grinding force for brittle materials considering co-existing of ductility and brittleness, Int. J. Adv. Manuf. Technol. 2016, 87, 1967–1975.

[15] Chang, H.C., Wang, J.J.J. A stochastic grinding force model considering random grit distribution, Int. J. Mach. Tools Manuf. 2008, 48, 1335–1344.

[16] Cheng, J.; Yin, G.; Wen, Q.; Song, H.; Gong, Y. Study on grinding force modelling and ductile regime propelling technology in micro drill-grinding of hard-brittle materials, J. Mater. Process. Technol. 2015, 223, 150–163.

[17] Xiao, X.; Zheng, K.; Liao, W.; Meng, H. Study on cutting force model in ultrasonic vibration assisted side grinding of zirconia ceramics, Int. J. Mach. Tools Manuf. 2016, 104, 58–67.

[18] Liu, D.; Cong, W.L.; Pei, Z.J.; Y. Tang. A cutting force model for rotary ultrasonic machining of brittle materials, Int. J. Mach. Tools Manuf. 2012, 52, 77–84.

[19] Zhang, J.H.; Li, H.; Zhang, M.L.; Zhao, Y.; Wang, L.Y. Study on force modeling considering size effect in ultrasonic-assisted micro-end grinding of silica glass and Al2O3 ceramic, Int. J. Adv. Manuf. Technol. 2017, 89, 1173–1192.

460 [20] Lee, S.H. Analysis of ductile mode and brittle transition of AFM nanomachining of silicon, J. Mach.
461 Tools Manuf. 2012, 61, 71–79.16
462 [21] Hertz, H.; Jones, D.E.; Schott, G.A. Miscellaneous Papers, Macmillan and Company, London, 1986.
463 [22] Son, S.M.; Lim, H.S.; Ahn, J.H. Effects of the friction coefficient on the minimum cutting thickness in
464 micro cutting. Int. J. Mach. Tools Manuf. 2005, 45, 529–535.
465 [23] Zhang, F.; Meng, B.; Geng, Y.; Zhang, Y.; Li, Z. Friction behavior in nanoscratching of reaction bonded
466 silicon carbide ceramic with Berkovich and sphere indenters, Tribol. Int. 2016, 97, 21–30.
467 [24] Agarwal, S.; Rao, P.V. Predictive modeling of force and power based on a new analytical undeformed
468 chip thickness model in ceramic grinding, Int. J. Mach. Tools Manuf. 2013, 65, 68–78.
469 [25] Zhang, W.; Subhash, G. An elastic-plastic-cracking model for finite element analysis of indentation
470 cracking in brittle materials, Int. J. Solids Struct. 2001, 38, 5893–5913.
471 [26] Arcona, C. and Th A. Dow. An empirical tool force model for precision machining. J. Manuf. Sci.
472 Eng.120 (1998): 700-707.
473 [27] Marshall, D.; Lawn, B.; Evans, A. Elastic/plastic indentation damage in ceramics: the lateral crack
474 system, J. Am. Ceram. Soc. 1982, 65, 561–566.
475 [28] Jing, X.; Maiti, S.; Subhash, G. A new analytical model for estimation of scratch-induced damage in
476 brittle solids, J. Am. Ceram. Soc. 2007, 90, 885–892.
477 [29] Malkin, S. Grinding Technology Theory and Applications of Machining with Abrasives, Northeastern
478 University Press, Shenyang, 2002.
479 [30] Hou, Z.B.; Komanduri, R. On the mechanics of the grinding process-Part I. Stochastic nature of the
480 grinding process, Int. J. Mach. Tools Manuf. 2003, 43. 1579–1593.